Entropy **2015**, *17*, 5304-5332; doi:10.3390/e17085304

OPEN ACCESS

entropy

ISSN 1099-4300

www.mdpi.com/journal/entropy

Article

Entropy Generation through Deterministic Spiral Structures in a Corner Boundary-Layer Flow

LaVar King Isaacson

Mechanical Engineering, University of Utah, 2067 Browning Avenue, Salt Lake City, UT 84108, USA; E-Mail: lkisaacson1@mac.com

Academic Editors: Morin Celine, Bernard Desmet and Fethi Aloui

Received: 5 April 2015 / Accepted: 22 July 2015 / Published: 27 July 2015

Abstract: It is shown that nonlinear interactions between boundary layers on adjacent corner surfaces produce deterministic stream wise spiral structures. The synchronization properties of nonlinear spectral velocity equations of Lorenz form yield clearly defined deterministic spiral structures at several downstream stations. The computational procedure includes Burg's method to obtain power spectral densities, yielding the available kinetic energy dissipation rates within the spiral structures. The singular value decomposition method is applied to the nonlinear time series solutions yielding empirical entropies, from which empirical entropic indices are then extracted. The intermittency exponents obtained from the entropic indices allow the computation of the entropy generation through the spiral structures to the final dissipation of the fluctuating kinetic energy into background thermal energy, resulting in an increase in the entropy. The entropy generation rates through the spiral structures are compared with the entropy generation rates within an empirical turbulent boundary layer at several stream wise stations.

Keywords: corner boundary-layer flows; deterministic spiral structures; empirical entropies; fractal intermittency exponents; entropy generation

1. Introduction

Corner boundary layer flows are found everywhere in our mechanical world. These types of flows occur in applications as different as square ducts in heating-cooling ventilation systems to the connections of aircraft wings to aircraft bodies. And yet, as discussed by Cebeci and Cousteix [1], the design of the connecting region of an aircraft wing to the aircraft fuselage is still primarily dependent upon the

results of wind tunnel testing. An improvement in the understanding of the fundamentals of corner boundary layer flows could provide better energy efficiency in the performance of many such flow devices.

In this article, we report the results of the application of a computational procedure to calculate the three-dimensional boundary layer flow in a right-angle corner flow environment. The development of the computational procedure begins with the observation that the stream wise velocity will form laminar boundary layers in the stream wise direction along both the horizontal surface and the vertical surface of the corner configuration. As the boundary layer forms along the vertical surface in the stream wise direction, it will produce a velocity normal to the vertical surface in the direction of the z-axis. This cross flow velocity will form a boundary layer profile in the z-y plane along the horizontal surface, acting as a cross flow input to the horizontal laminar boundary layer which forms in the x-y plane. We have found that this cross flow velocity and resulting velocity profile are key elements in the triggering of deterministic spiral structures in the corner boundary layer flow.

This article includes the following sections:

In Section 2, we discuss the thermodynamic and transport processes computed for the products of combustion of a methane-air mixture in a steady flow combustion process. These thermo-transport properties are used throughout the computational processes. In Section 3, we assume that our flow environment is a three-dimensional laminar flow in the stream wise direction in a right-angle corner configuration. We assume a constant velocity in the stream wise (along the x-axis) direction, with no pressure gradient, and that the flow is incompressible. We assume that laminar boundary layers are formed in the stream wise direction along both the horizontal surface and along the vertical surface. The formation of the boundary layer along the vertical surface provides the cross flow velocity that forms the laminar boundary layer in the z-direction orthogonal to the x-y plane boundary layer profile. In Section 4, the Townsend equations [2] are written for the three fluctuating velocity components within this three-dimensional boundary layer flow. These equations are Fourier transformed into a set of coupled nonlinear deterministic equations of Lorenz form. The synchronization properties of Lorenz type equations are used to extract deterministic spiral structures. Section 5 discusses the solution of these equations for the time-dependent behavior of the both the Fourier components of the wave number vectors and the Fourier components of the fluctuating velocity wave vectors. The power spectral densities of the resulting non-linear solutions are obtained by Burg's method and are presented in Section 6. The results for the singular value decomposition of selected regions of the nonlinear time series solutions for the normal and span wise spectral velocity wave components are presented in Section 7. From these results, empirical entropy is defined for each of the empirical modes for each velocity wave component obtained in the computation. In Section 8, the empirical entropic index is computed from the empirical entropy value for each empirical mode. Section 9 presents the intermittency exponent obtained from the associated empirical entropic index for each empirical mode of the singular value decomposition process. Section 10 presents the calculation of the entropy generation rate through the dissipation of the kinetic energy applied as input to the original deterministic spiral structures produced within the three-dimensional boundary layer environment. The article closes with a discussion of the results and final conclusions.

2. Combustion Chamber Environment

The flow configuration we are approximating in this exploratory study is shown in Figure 1. The figure is intended to represent the corner flow in the entrance to a square duct in, for example, an industrial heating unit. In this section, we describe the characteristics of the working gas we use in our computational procedure. In the next section, we will fully describe the three-dimensional corner boundary layer configuration shown in Figure 1.

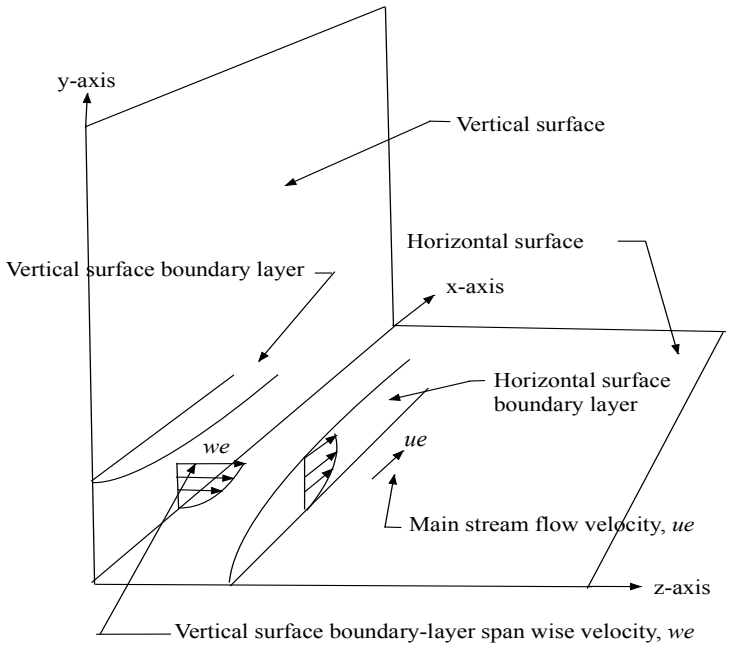

Figure 1. Schematic of the interacting boundary layers in a corner flow is shown.

The working gas is assumed to be the initial combustion of methane with 100 per cent theoretical air. Excess air is then supplied, providing a total of 300 percent theoretical air to the combustion process. The products of the combustion process consist of 3.38 percent CO_2, 6.77 percent H_2O, 13.53 percent O_2 and 76.32 percent N_2, with percent by volume. The initial temperature is taken as 298.15 K, with the pressure assumed to be 1 atm (101.325 kPa). The adiabatic flame temperature for these conditions is 1140.0 K. Dissociation of the products is neglected. The transport properties for this mixture of polyatomic gases are determined by the procedures presented in Dorrance [3], including the Wilke approximation for mixtures of polyatomic gaseous species. The primary parameter required for the computation of both the set of steady boundary layer equations and the time-dependent deterministic equations is the kinematic viscosity. The working gas chosen for this study provides a value of kinematic viscosity that readily yields instabilities in the computational process. The thermodynamic and transport properties used throughout the computational procedure are as follows:

$$\text{Inlet temperature, } t_i\text{: } 298.15 \text{ K} \tag{1}$$

$$\text{Adiabatic flame temperature, } T_{aft}\text{: } 1140.0 \text{ K} \tag{2}$$

$$\text{Static pressure, } p_1\text{: } 1.013 \times 10^5 \text{ N/m}^2 \tag{3}$$

$$\text{Kinematic viscosity, } \nu_1\text{: } 1.523 \times 10^{-4} \text{ m}^2/\text{s} \tag{4}$$

3. Boundary-Layer Development

The computational procedure used in the determination of the time-dependent characteristics of the flow in the initial region of a corner boundary layer environment, is dependent on the values of the mean velocity gradients across the three-dimensional boundary layers in the corner flow. These mean velocity gradients are determined separately from the coupled nonlinear equations for the fluctuating components.

The development of the stream wise boundary layer along the vertical surface of the corner that provides the crosswind velocity, w_e, normal to the boundary layer profile in the x-y plane, is shown in Figure 1. It is this crosswind velocity itself that develops the appropriate boundary layer profile in the z-y plane for inclusion in our computational procedure. The magnitude of this crosswind velocity, w_e, serves as the triggering mechanism for the development of deterministic spiral structures in the corner boundary layer flow process.

We use a Runge-Kutta computational procedure presented by Chow [4] to calculate the normal velocity, w_e in the z-direction, generated by the stream wise Blasius boundary layer on the vertical surface, as shown in Figure 1. The value of w_e for each stream wise station is computed for a normalized distance of 8.0 from the vertical surface at that x-axis station. The resulting crosswind velocities are shown in Figure 2 as a function of the normalized distance from the surface, η, as defined in Equation (9).

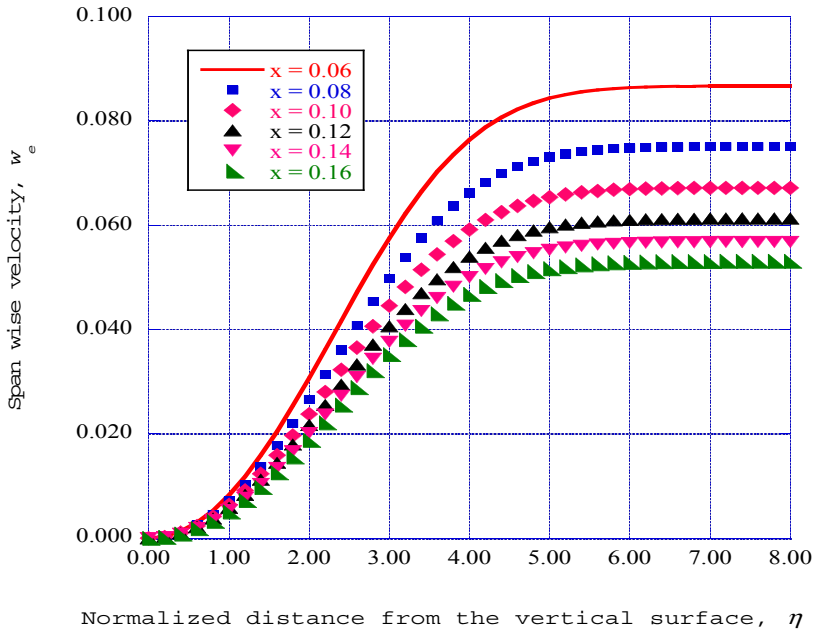

Figure 2. The span wise (crosswind) velocity produced by the stream wise boundary layer along the vertical surface is shown for several locations along the x-axis.

The three-dimensional boundary layer configuration consists of the boundary layer produced by the stream wise velocity, u_e, in the stream wise direction, providing the velocity profiles in the x-y plane, while the boundary layer produced by the crosswind velocity, w_e, provides the velocity profiles in the z-y plane. Hansen [5] has indicated that boundary layer profiles in an orthogonal coordinate system possess the characteristic of similarity allowing for the introduction of the Falkner-Skan transformation

(Cebeci and Bradshaw [6]). Hansen [5] has also provided a sketch of the orthogonal configuration of the boundary layer system that we employ in this study.

Cebeci and Bradshaw [6] present computer source codes for the numerical solutions for both laminar and turbulent boundary layers over horizontal surfaces. The equations required for the laminar boundary layer mean velocity gradients have been presented in [7]. The mean boundary-layer velocity gradients serve as control parameters for the time-series solutions of the coupled, non-linear Lorenz-type equations for the fluctuating spectral wave number components and the spectral velocity wave components.

A summary of the essential equations used by Cebeci and Bradshaw [6] that form the basis of the Keller-Cebeci box method for solution of the boundary layer equations is presented. The momentum equation for the steady stream wise boundary-layer flow, including contributions from both laminar and turbulent flows, is written as:

$$u\frac{\partial u}{\partial x}+v\frac{\partial u}{\partial y}=-\frac{1}{\rho}\frac{dp}{dx}+\frac{1}{\rho}\frac{\partial}{\partial y}\left[\mu\frac{\partial u}{\partial y}-\rho\overline{u'v'}\right]. \tag{5}$$

The definitions of the terms in this equation are found in the Nomenclature.

The boundary conditions for this equation are

$$y=0 \qquad u=v=0 \tag{6}$$

$$y=\delta(x) \qquad u=u_e(x) \tag{7}$$

The Reynolds shear stress for the computation of turbulent boundary layers is modeled with the "eddy viscosity", ε_m, having the dimensions of (viscosity)/(density), by

$$-\rho\overline{u'v'}=\rho\varepsilon_m\frac{\partial u}{\partial y} \tag{8}$$

The Falkner-Skan transformation used by Cebeci and Bradshaw [6] is

$$\eta=\left(\frac{u_e}{\nu x}\right)^{1/2}y \tag{9}$$

For the general case, the velocity at the edge of the boundary layer, $u_e=u_e(x)$, is assumed to vary with distance x. In our computations, we consider only the case of a constant free stream velocity with a zero stream wise pressure gradient.

The dimensionless stream function, $f(x,\eta)$, is defined by

$$\Psi(x,y)=(u_e\nu x)^{1/2}f(x,\eta). \tag{10}$$

These definitions yield the results for the mean boundary layer velocities *u* and *v* as

$$u=u_e f' \qquad v=-\frac{\partial}{\partial x}\left[(u_e\nu x)^{1/2}f\right]+\frac{\eta}{2}\left(\frac{u_e\nu}{x}\right)^{1/2}f' \tag{11}$$

Differentiation with respect to η is indicated by the prime in these expressions.

From Bernoulli's equation, the pressure gradient term is given by $\frac{dp}{dx}=-\rho u_e\frac{du_e}{dx}$. To simplify the resulting equations, the parameter *m* is defined as

$$m = \frac{x}{u_e}\frac{du_e}{dx} \tag{12}$$

The transformed mean momentum equation for the thin plane shear layer is written as [6]:

$$\left((1+\frac{\varepsilon}{\nu})f''\right)' + \frac{m+1}{2}ff'' + m\left[1-(f')^2\right] = x\left(f'\frac{\partial f'}{\partial x} - f''\frac{\partial f}{\partial x}\right) \tag{13}$$

With no surface mass transfer, the boundary conditions for Equation (13) are,

$$f(x,0) = 0 \tag{14}$$

$$f'(x,0) = 0 \qquad \lim_{\eta\to\infty} f'(x,\eta) = 1 \tag{15}$$

The computer solution procedures for this third-order differential equation, as developed by Cebeci and Bradshaw [6], replace the third-order differential equation, Equation (13), with three first-order differential equations in the following fashion:

$$f' = u \tag{16}$$

$$u' = v \tag{17}$$

$$((1+\frac{\varepsilon}{\nu})v)' + \left(\frac{m+1}{2}\right)fv + m(1-u^2) = x\left(u\frac{\partial u}{\partial x} - v\frac{\partial f}{\partial x}\right) \tag{18}$$

The corresponding boundary conditions for these equations are

$$f(x,0) = 0 \qquad u(x,0) = 0 \qquad u(x,\eta_\infty) = 1 \tag{19}$$

In Equation (17), v is not the y-component velocity. The gradients for the boundary layer mean velocity components are obtained from the computational results for both the stream wise boundary layer and the span wise boundary layer on the horizontal surface [7]. These gradients serve as control parameters for the solution of the nonlinear time-dependent Townsend equations for the fluctuating spectral velocity wave components in the boundary layer environment.

The similarity of the laminar boundary layers along the starting locations for the x-y and z-y planes allows the computation of the laminar mean velocity profiles in both the x-y and the z-y planes. The mean laminar velocity profiles in the z-y plane are computed at the span wise station, z = 0.003, with the mean velocity profiles in the x-y plane computed at various stream wise stations from x = 0.06 to x = 0.16.

4. Equations of Lorenz Form for the Spectral Velocity Wave Components

4.1. Development of the Time Dependent Spectral Equations

The crosswind velocity produced by the stream wise boundary layer along the vertical surface will trigger instabilities through nonlinear interactions among the stream wise velocity fluctuations and the span wise and normal velocity fluctuations within the horizontal laminar boundary layer flow. A set of equations for these velocity fluctuations, separate from the equations for the steady boundary layer flow, may be obtained through the methods of Townsend [2]. Separating the equations of motion into steady and unsteady equations, the equations for the velocity fluctuations may then be written as [2,8]:

$$\frac{\partial u_i}{\partial t} + U_j \frac{\partial u_i}{\partial x_j} + u_j \frac{\partial U_i}{\partial x_j} + u_j \frac{\partial u_i}{\partial x_j} = -\frac{1}{\rho}\frac{\partial p}{\partial x_i} + \nu \frac{\partial^2 u_i}{\partial u_j \partial u_j} \tag{20}$$

In these equations, ρ is the density and v is the kinematic viscosity, U_i represent the mean boundary layer velocity components with i = 1, 2, 3 indicating the x, y, and z components, and x_j, with j = 1, 2, 3, designate the x, y and z directions. The pressure term is eliminated by taking the divergence of Equation (20) and invoking incompressibility, yielding:

$$-\frac{1}{\rho}\frac{\partial^2 p}{\partial x_l^2} = 2\frac{\partial U_l}{\partial x_m}\frac{\partial u_m}{\partial x_l} + \frac{\partial u_l}{\partial x_m}\frac{\partial u_m}{\partial x_l} \tag{21}$$

The equations for the velocity and pressure fluctuations represent the variables of interest in the physical plane. However, the computational procedures require the equations to be in the spectral plane. The solution of the spectral equations yields the fluctuating wave vector components and the fluctuating velocity wave components. Through Parseval's theorem, the quadratic of the spectral fluctuating velocity components also represents the quadratic of the corresponding fluctuating velocity components in the physical plane. The quadratic terms in the physical plane represent the kinetic energy residing in the respective fluctuating velocity components. The ultimate dissipation rate of this kinetic energy into background thermal internal energy provides the entropy generation rate within the boundary layer deterministic spiral structures.

The fluctuating velocity and pressure fields of Equations (20) and (21) are expanded in terms of the Fourier components [8]:

$$u_i(x,t) = \sum_k a_i(k,t)\exp(ik \bullet x) \tag{22}$$

and

$$\frac{p(x,t)}{\rho} = \sum_k b(k,t)\exp(ik \bullet x) \tag{23}$$

The pressure component in Equation (20) is transformed into a function of fluctuating velocity wave components and boundary layer velocity gradients through Equations (22) and (23). Substituting the resulting equations and Equation (22) into Equation (20) yields an expression for the fluctuations of the velocity wave vector components with time. The resulting equations for the three spectral velocity wave components, $a_i(k)$, are then given as:

$$\frac{da_i(k)}{dt} = -\nu k^2 a_i(k) - \frac{\partial U_i}{\partial x_i}a_i(k) + 2\frac{k_i k_l}{k^2}\frac{\partial U_l}{\partial x_m}a_i(k) + i\sum_{k'+k''=k}(k_l\frac{k_i k_m}{k^2} - \delta_{im}k_l)a_l(k')a_m(k'') \tag{24}$$

The time-series solutions for the wave numbers, k_i are obtained from the general equations for the balance of transferable properties:

$$\frac{dk_i}{dt} = -\frac{\partial U_l}{\partial x_i}k_l \tag{25}$$

The set of equations for the time-dependent wave number components, including the gradients of the mean velocities in the x-y and z-y boundary layers, may be written from Equation (25) as:

$$\frac{dk_x}{dt} = -\frac{\partial U}{\partial x}k_x - \frac{\partial V_x}{\partial x}k_y \tag{26}$$

$$\frac{dk_y}{dt} = -\frac{\partial U}{\partial y}k_x - \frac{\partial V_x}{\partial y}k_y - \frac{\partial W}{\partial y}k_z \tag{27}$$

$$\frac{dk_z}{dt} = -\frac{\partial V_z}{\partial z}k_y - \frac{\partial W}{\partial z}k_z \tag{28}$$

The nonlinear products of the fluctuating spectral velocity wave components in Equations (24) are retained in our series of equations by characterizing the coefficients

$$k_l(\delta_{im} - \frac{k_i k_m}{k^2}) \tag{29}$$

as a projection matrix (Mathieu and Scott [8]). This coefficient represents the projection of a given velocity wave vector component, a_i, normal to the direction of the corresponding wave number component, k_i. A model equation for this expression in the form

$$(1 - K \times \cos(k(t))) \tag{30}$$

is introduced to retain the effect of the projection matrix on the nonlinear interactive terms in our equations. K is an empirical weighting amplitude factor [7] and $k(t)$ is given by:

$$k(t) = \sqrt{(k_x^2)} \tag{31}$$

The weighting factor, Equation (30), has been used by Manneville [9] to obtain pattern formations for simple configurations and by Pyragas [10] as a weighting factor to control chaos by internal feedback control. The transfer matrix, Equation (29), is replaced in Equations (24) by the expression $(1 - F)$, where F is defined as:

$$F = K \times \cos(k(t)) \tag{32}$$

The three deterministic equations for the spectral velocity wave vectors may then be written as:

$$\frac{da_{xn}}{dt} = \sigma_{yn}a_{yn} - \sigma_{xn}a_{xn} \tag{33}$$

$$\frac{da_{yn}}{dt} = -(1-F)a_{rn}a_{zn} + r_n a_{xn} - s_n a_{yn} \tag{34}$$

$$\frac{da_{zn}}{dt} = (1-F)a_{rn}a_{yn} - b_n a_{zn} \tag{35}$$

In Equations (33)–(35), the respective time-dependent coefficients of the spectral velocity wave components at the stream wise station n have the following forms:

$$\sigma_{yn} = \left[\left(\frac{2k_x k_x}{k^2} - 1\right)\frac{\partial U}{\partial y} + \frac{2k_x k_y}{k^2}\frac{\partial V_x}{\partial y} + \frac{2k_x k_z}{k^2}\frac{\partial W}{\partial y}\right] \tag{36}$$

$$\sigma_{xn} = \left\{\nu k^2 - \left[\left(\frac{2k_x k_x}{k^2} - 1\right)\frac{\partial U}{\partial x} + \frac{2k_x k_y}{k^2}\frac{\partial V_x}{\partial x} + \frac{2k_x k_z}{k^2}\frac{\partial W}{\partial x}\right]\right\} \tag{37}$$

$$r_n = \left[\frac{2k_y k_x}{k^2}\frac{\partial U}{\partial x} + \left(\frac{2k_y k_y}{k^2} - 1\right)\frac{\partial V_x}{\partial x} + \frac{2k_y k_z}{k^2}\frac{\partial W}{\partial x}\right] \tag{38}$$

$$s_n = \left\{\nu k^2 - \left[\frac{2k_y k_x}{k^2}\frac{\partial U}{\partial y} + \left(\frac{2k_y k_y}{k^2} - 1\right)\frac{\partial V_z}{\partial y} + \frac{2k_y k_z}{k^2}\frac{\partial W}{\partial y}\right]\right\} \tag{39}$$

$$b_n = \left\{ \nu k^2 - \left[\frac{2k_z k_x}{k^2} \frac{\partial U}{\partial z} + \frac{2k_z k_y}{k^2} \frac{\partial V_z}{\partial z} + \left(\frac{2k_z k_z}{k^2} - 1 \right) \frac{\partial W}{\partial z} \right] \right\} \quad (40)$$

The internal feedback parameter $(1-F)$ is applied to the nonlinear terms in the equations for $\frac{da_y}{dt}$ and $\frac{da_z}{dt}$, Equations (34) and (35), and not to the directly accessible dependent variables. The application of the feedback parameter in this fashion implies that the nonlinear terms in the first-order equations for the spectral velocity wave vector fluctuations represent a "pumping" process, transferring energy from the stream wise spectral velocity wave vector, a_x, into the normal velocity wave vector, a_y, and the span wise velocity wave vector, a_z.

The value of K used in the computational procedure is the empirical value that yields unstable solutions for the fluctuating spectral velocity wave components within the laminar boundary layer flow. We have found that a value of $K = 0.05$ yields the prediction of boundary layer instabilities for the particular value of kinematic viscosity given in Equation (4).

The solutions of the "modified Townsend equations", Equations (33) through Equation (40), are obtained by including the expressions for the mean boundary layer velocity gradients, the feedback parameter for the nonlinear coupling terms, and the solutions for the spectral wave number components. Arranging these equations into Lorenz form yields a set of coupled nonlinear time-dependent first-order differential equations. The mean boundary-layer velocity gradients, the gas mixture kinematic viscosity and the feedback parameter serve as control parameters for the solutions of both the set of equations for the spectral wave numbers and the set of Lorenz-type modified Townsend equations.

4.2. Computational Results for the Transmitter Station

The set of spectral wave number equations and the set of modified Townsend equations are first solved for an initial station at the stream wise location of x = 0.06. The mean velocity gradients computed for the steady three-dimensional laminar boundary layers at this station serve as control parameters. Then the complete set of equations, including the steady boundary layer equations, the spectral wave number equations, and the modified Townsend equations, are solved at five separate locations along the x-axis, at x = 0.08, x = 0.10, x = 0.12, x = 0.14, and x = 0.16, downstream of the initial station.

The solution of the overall set of equations at the initial station involves the internal feedback parameter (1 − F) in the solution. The solution at this station initiates the instability process. The internal feedback parameter is not used for the solution at the next location, being replaced by the stream wise spectral velocity output from the initial station. This provides the basis for designation of the initial station as the "transmitter" station.

The synchronization properties of the Lorenz equations, as described in the next section, are used to extract deterministic structures from the nonlinear time series solutions for each station. These downstream stations are therefore designated as "receiver" stations. This nomenclature comes from communications theory. Each receiver station will have its own set of steady boundary layer velocity gradients as input control parameters for the solution of the overall set of six simultaneous equations applicable at that particular station.

The solutions of Equations (33)–(35) yield the fluctuating spectral velocity wave components for the transmitter station at the stream wise location x = 0.06 and the span wise location of z = 0.003.

The outer edge of the boundary layer is assumed to be at the normalized distance $\eta_e = 8.00$, with the boundary layer instability observed within the boundary layer at a normalized distance from the horizontal surface of approximately $\eta = 3.0$.

The solutions of nonlinear, coupled differential equations such as the Lorenz equations are sensitive to the choice of initial conditions. We have found consistent solutions with initial values for the spectral wave number components of $k_x[1] = 0.04$, $k_y[1] = 0.02$ and $k_z[1] = 0.02$, while the initial conditions for the velocity wave components are $a_x[1] = 0.20$, $a_y[1] = 0.01$ and $a_z[1] = 0.001$. For the kinematic viscosity given in Equation (4), the weighting factor that yields flow instabilities has been found to be $K = 0.05$.

Computer source codes have been presented by Press *et al.* (pp. 714–720 [11]) for the integration of Equations (33)–(35). The method uses a fifth-order Runge-Kutta technique. The time step is 0.0001 s using 12,288 steps over the total time frame for the integration process. The time series solution for each spectral velocity wave vector component is saved to disc for processing to extract various statistical properties of the deterministic spiral structures represented in the nonlinear time series solutions.

Figure 3 presents the fluctuating stream wise spectral velocity wave component, a_{x0}, for the transmitter station, $n = 0$, as a function of the time step number over the total time range of the integration process. Figure 4 shows the phase diagram of a_{x0}-a_{y0}, where a_{y0} is the normal spectral velocity wave component solution for the transmitter station. Figure 5 shows the corresponding phase diagram for a_{z0}-a_{y0}, where a_{z0} is the span wise spectral velocity wave component, again for the transmitter station. A three-dimensional representation of the computed spectral velocity wave components is shown in Figure 6.

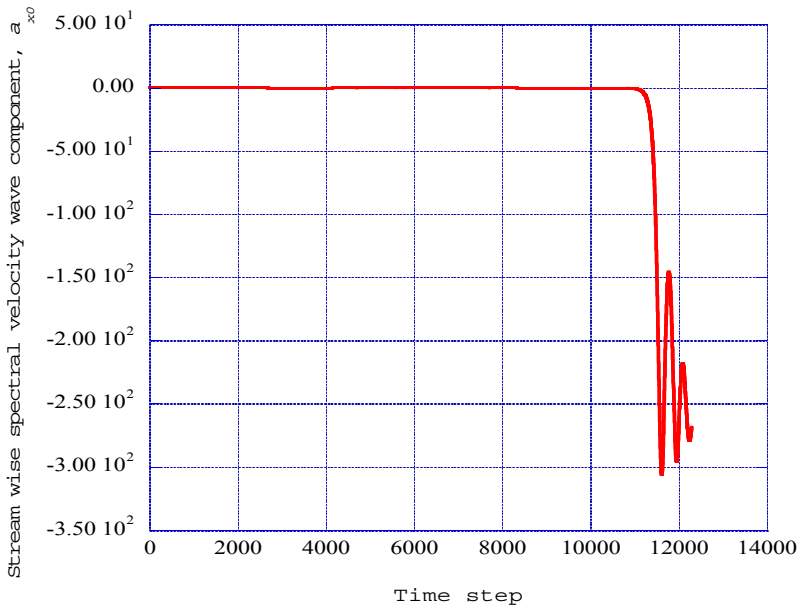

Figure 3. The stream wise spectral velocity wave component, a_{x0}, is shown as a function of time step number at the transmitter station x = 0.06.

These results indicate that the time-dependent nonlinear time-series solutions of the coupled nonlinear deterministic equations within the transmitter station yield the initiation of stream wise deterministic spiral structures. A significant observation is that the crosswind velocity, w_e, serves as a triggering

mechanism for the initiation of the instability. When the value of the crosswind velocity at the transmitter station (x = 0.06), is less than 0.083, no instability is observed. However, when the crosswind velocity reaches 0.083, a slight instability is observed. The results shown in Figures 3 through 6 were obtained with a crosswind velocity of 0.0867, the value obtained from the Blasius solution for the stream wise boundary layer at x = 0.06 along the vertical surface.

As the laminar boundary layer along the vertical surface develops in the x-direction, the crosswind velocity, w_e, produced by this boundary layer decreases in magnitude. This effect is shown in detail in Figure 2. These values of the crosswind velocity, w_e, are used for the computation of the solutions of the modified Townsend equations at each respective receiver station, as described in the next section.

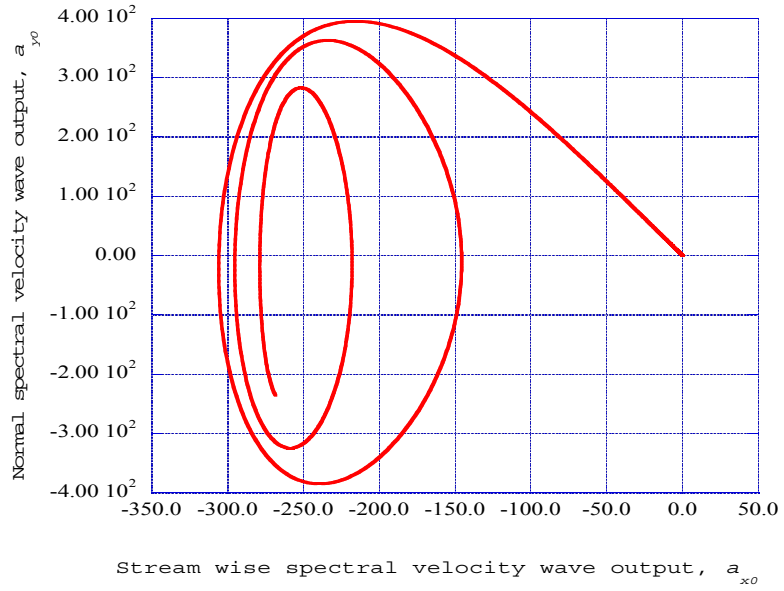

Figure 4. The phase diagram of the stream wise and normal spectral velocity components, a_{x0}-a_{y0}, is shown for the transmitter station x = 0.06.

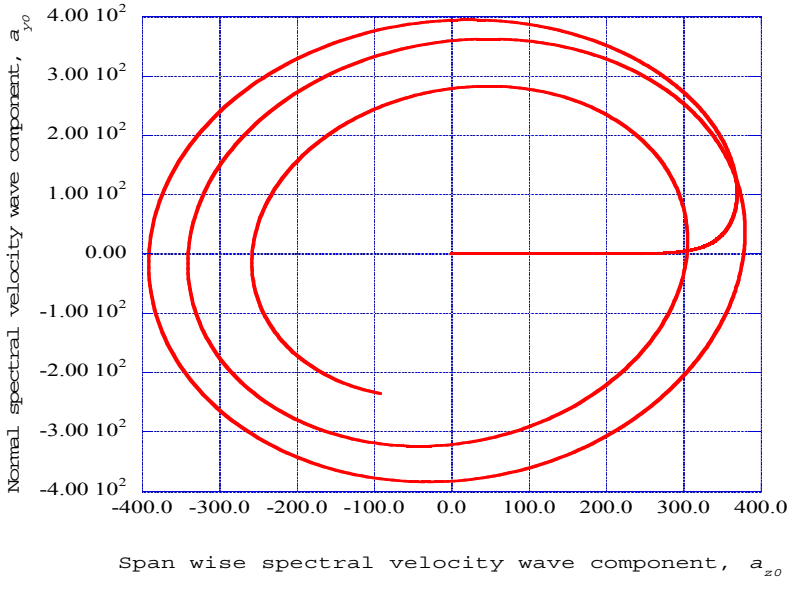

Figure 5. The phase diagram of the span wise and normal spectral velocity components, a_{z0}-a_{y0}, is shown for the transmitter station x = 0.06.

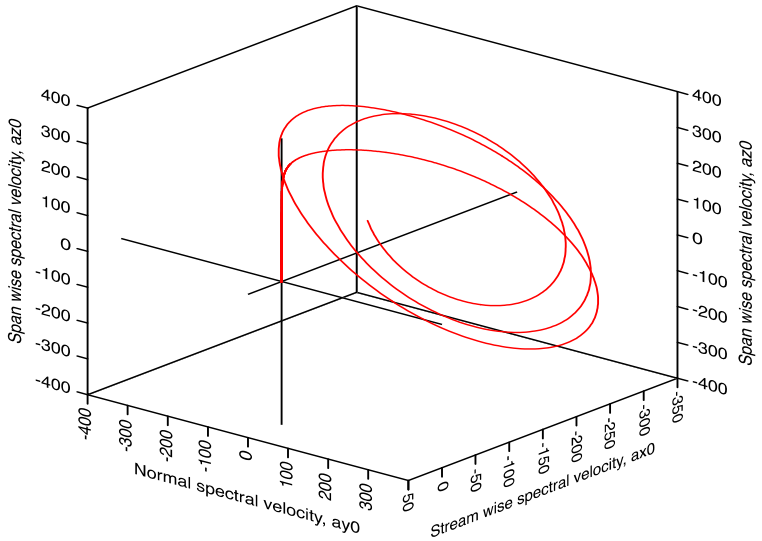

Figure 6. A three-dimensional representation of the stream wise, normal and span wise spectral velocity components is shown for the transmitter station x = 0.06.

4.3. Extracting Ordered Signals from Nonlinear Instability Time Series

Pecora and Carroll [12], Pérez and Cerdeiral [13] and Cuomo and Oppenheim [14] present methods for extracting messages that are masked by chaotic signals through the synchronization properties of systems of Lorenz-type equations. The synchronization properties of Lorenz-type equations are adapted here to extract ordered signals from the nonlinear time series generated for each of the computational stations.

The nonlinear time series solutions for the initial Lorenz system, designated as the transmitter station, are obtained for the particular mean boundary layer velocity profiles computed at the x-axis station of x = 0.06. The mean boundary layer velocity gradients for each of the receiver systems at each respective x-axis location are computed in the same manner as for the transmitter system. Thus, each receiver system has a set of input control parameters unique to its position along the x-axis. Following the results in [15], the output for the stream wise velocity wave component from the transmitter station, a_{x0}, provides the input to the first receiver station. The input to the next receiver station is then made up of the sum of the stream wise velocity component output from the transmitter station plus the corresponding output from the first receiver station. This process is repeated over each of the remaining four receiver stations to monitor the generation of deterministic spiral structures within the developing three-dimensional boundary layer configuration for each x-axis position.

For each stream wise station, *n,* the system of nonlinear dynamic equations is written as:

$$\frac{da_{xn}}{dt} = \sigma_{yn} a_{yn} - \sigma_{xn} a_{xn} \tag{41}$$

$$\frac{da_{yn}}{dt} = -a_{rn} a_{zn} + r_n a_{xn} - s_n a_{yn} \tag{42}$$

$$\frac{da_{zn}}{dt} = a_{rn} a_{yn} - b_n a_{zn} \tag{43}$$

Note that for the initial station, characterized as the transmitter station, a_{x0}, is the time-dependent spectral velocity wave component output from the transmitter station. The input driving term for the next station, the first receiver station, is then given by

$$a_{r1} = a_{x0} \tag{44}$$

where a_{x0} is the output from the initial or transmitter station.

In Equations (41)–(43), the input driving signal, a_{rn}, carrying information from the transmitter and the previous receiver stations to the n-th station is given by

$$a_{rn} = \sum_{i=0}^{i=n} a_{xi} \tag{45}$$

The initial value for the fluctuating stream wise spectral velocity wave vector component for the transmitter system is set equal to 0.200, while the initial value for the corresponding variable for each successive receiver system is set equal to 0.100. Lower initial values for the receiver systems result in much lower levels for the output signal of each of the receiver systems. This process determines the result that the outputs from each of the receiver systems will be masked by the original transmitter output signal, and that the synchronization process will yield an indication of the ordered regions within the transmitter signal.

4.4. Computational Results for the Receiver Stations

Figure 7 shows the stream wise spectral velocity component, a_{x3}, as a function of the time step for the third receiver station at x = 0.12. Figure 8 shows the a_{x3}-a_{y3} phase plane results obtained from the output of the third receiver station. Figure 9 shows the a_{z3}-a_{y3} phase plane results for this receiver. The processing of the input signal by the receiver system has resulted in a shifting of the orientation of the phase plane results for both sets of results from that indicated for the transmitter system. It is interesting that the synchronization process has introduced a reversal in the direction of the spiral structures just prior to time step of 12,000. Figure 10 presents a three-dimensional representation of the deterministic spiral structures for the third receiver station.

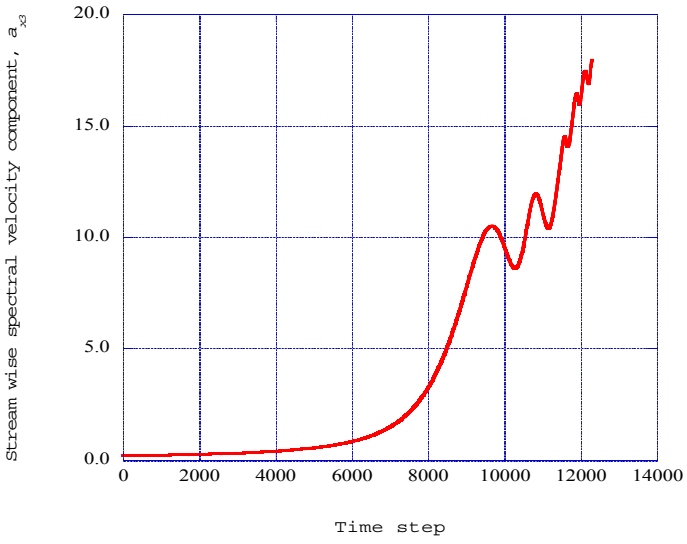

Figure 7. The stream wise spectral velocity component, a_{x3}, is shown as a function of the time step for the third receiver station at x = 0.12.

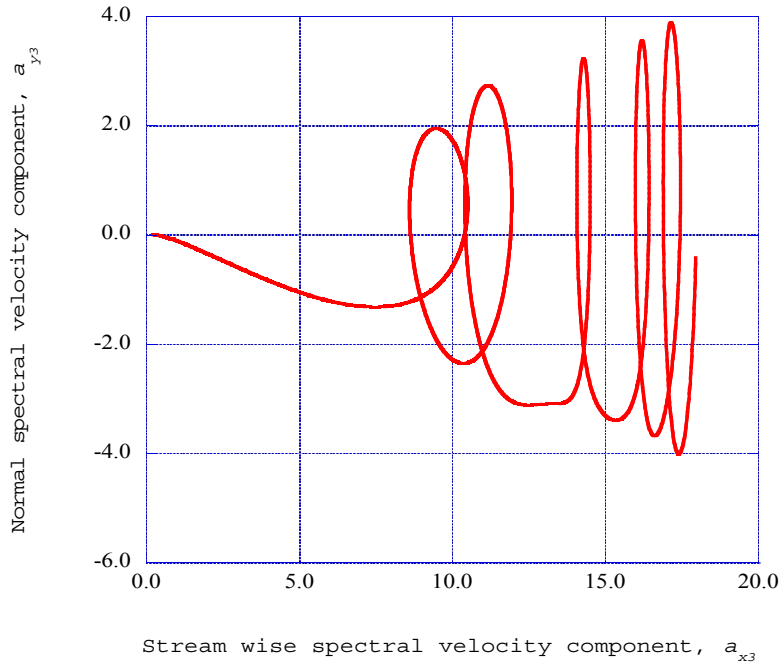

Figure 8. The phase plane for the spectral velocity components, a_{x3}-a_{y3}, for the third receiver station is shown for the x-axis location at x = 0.12.

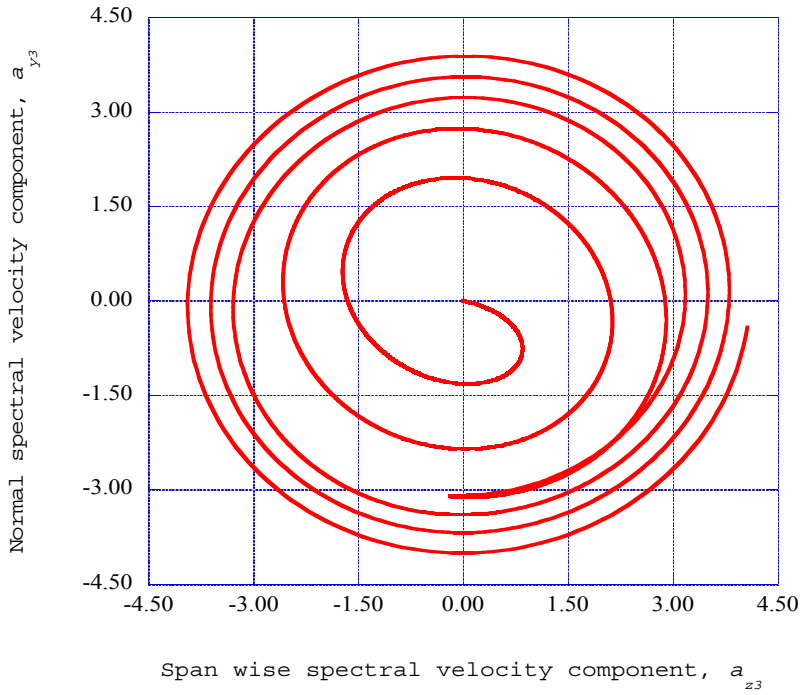

Figure 9. The phase plane for the spectral velocity components, a_{z3}-a_{y3}, for the third receiver station is shown for the x-axis location at x = 0.12.

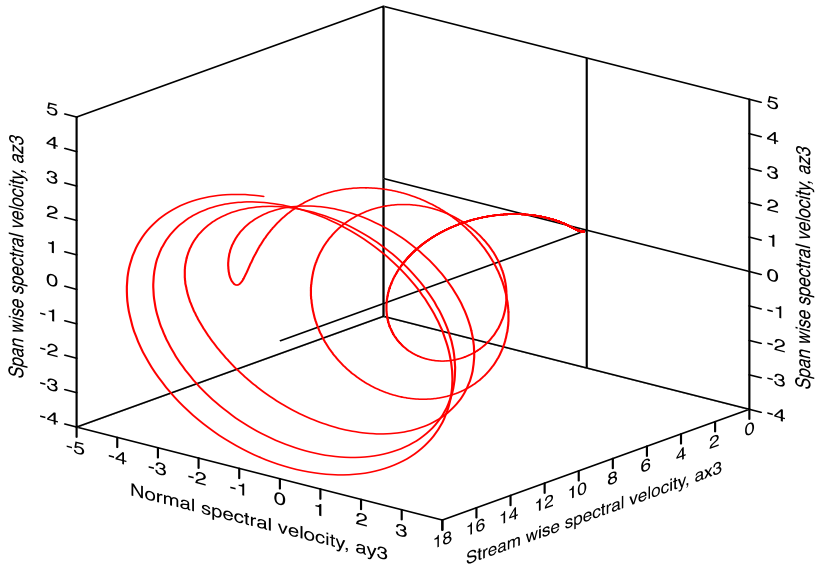

Figure 10. A three-dimensional representation of the stream wise, normal and span wise spectral velocity components is shown for the third receiver station at the x-axis location at x = 0.12.

5. Power Spectral Density within the Deterministic Spiral Structure

The Lorenz synchronization procedure yields the nonlinear time series solution for each of the five receiver stations in the stream wise direction. These solutions indicate the generation of deterministic spiral structures. To obtain the entropy generation rates through these structures, it is necessary to extract the underlying structural characteristics of the nonlinear time series solutions. Chen [16] describes the implementation of the maximum entropy method (Burg's method) for spectral analysis of geophysical seismic time data records.

A significant advantage of Burg's method is the enhancement of the spectral peaks in the power spectral density distribution. Press *et al.* (pp. 572–575 in [11]) present computer source codes for the prediction of the power spectral density using the maximum entropy method. The power spectral density for each of the spectral velocity wave component time series is computed for 1024 time step data samples from time step of 11,264 to time step 12,288. The selected time series is divided into 32 segments with 32 data sets per segment. Burg's method [16] is then applied to each segment of the 32 data sets to obtain 16 spiked values of the power spectral density for each of the stream wise, normal, and span wise spectral velocity wave components over the selected time series.

An indication that the instabilities obtained from the computational procedures are deterministic spiral structures is that power spectral density computation for the stream wise spectral velocity wave component yields a zero value for each of the stream wise stations. As shown in Figure 7, the stream wise velocity wave component seems to be a smooth function of the time step number. We also find that the computational procedures for the empirical entropy, empirical entropic index, and intermittency exponents do not apply to the stream wise spectral velocity wave component. It appears that the stream wise velocity component may be a reversible and adiabatic process, predicted by the solution of the Lorenz-form of the spectral fluctuation equations, with the mean boundary layer velocity profiles as control parameters. Therefore, the results that we report for the third receiver

station at x = 0.12 thus include only the time series solutions for the fluctuating normal and span wise spectral velocity wave components.

The resulting power spectral density results for the normal and span wise spectral velocity wave components for deterministic spiral structures for the third receiver station, at x = 0.12, are presented in Figures 11 and 12. Very fine grids are required to extract these results. We have assigned empirical mode numbers to these peaks, starting with mode $j = 1$ representing the highest peak in the distribution, continuing to mode $j = 16$, representing the corresponding lowest peak among the sixteen peaks.

The results shown in Figures 11 and 12 for the power spectral densities indicate that the kinetic energy available for dissipation is distributed in well-defined spectral peaks. The kinetic energy dissipation rate [8] for each power spectral density empirical mode is determined with the relation

$$E_{avail} = \int_{f_1}^{f_2} 2\nu(\frac{2\pi}{u_e})^3 f^2 E(f) df \tag{46}$$

Simpson's integration rule is used to obtain the kinetic energy dissipation rate for each of the power spectral density empirical modes. The total spectral energy dissipation rate is then obtained as the sum of the individual contributions across the modes. This value is then used to get the fraction of dissipation energy rate in each mode that is available for dissipation into internal energy.

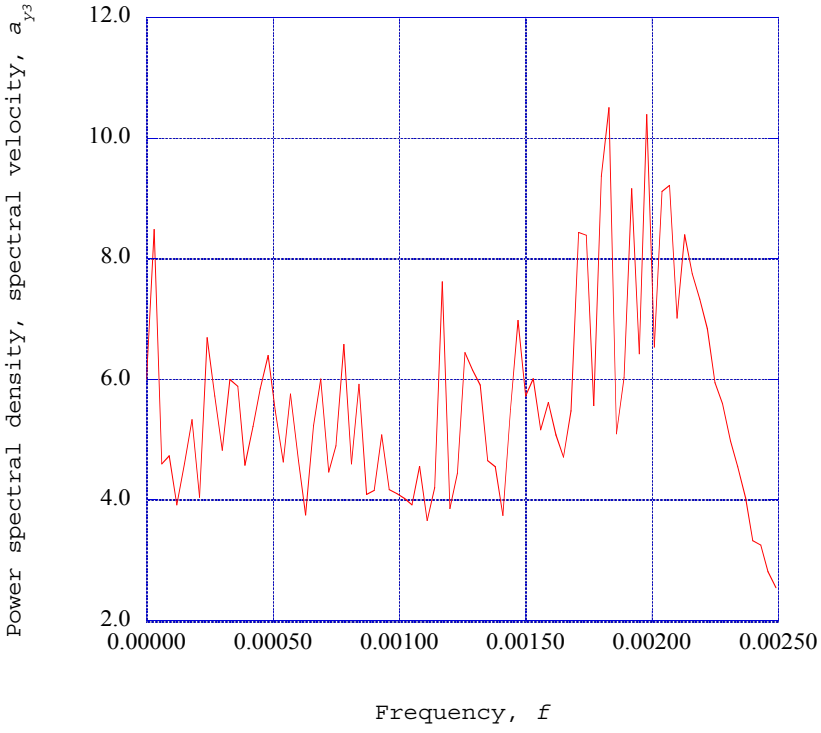

Figure 11. The power spectral density for the normal spectral velocity component, a_{y3}, is shown as a function of frequency for the third receiver station at the x-axis location x = 0.12.

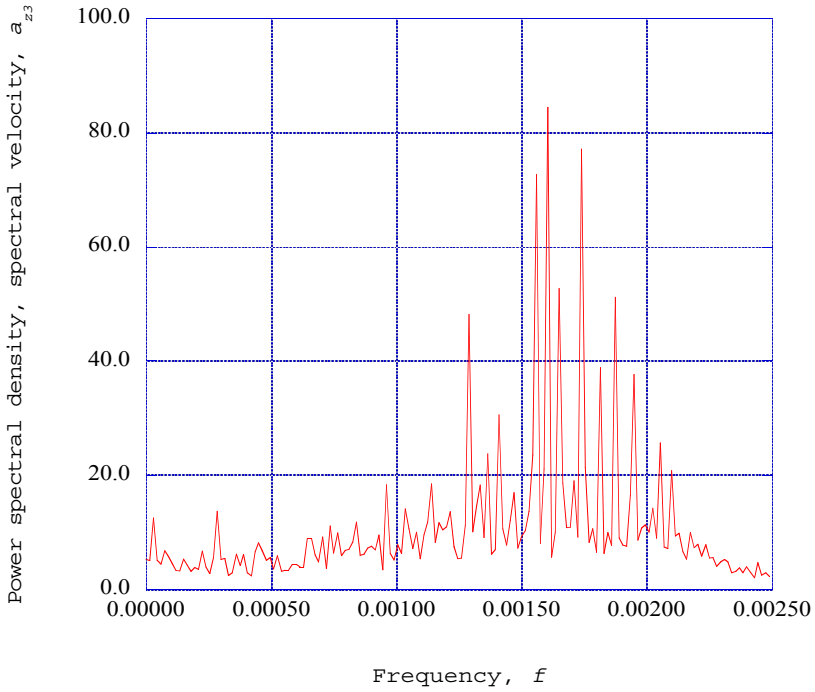

Figure 12. The power spectral density for the span wise spectral velocity component, a_{z3}, is shown as a function of frequency for the third receiver station at the x-axis location x = 0.12.

6. Singular Value Decomposition and Empirical Entropy

The singular value decomposition procedure can serve as a means of identifying fundamental characteristics of the nonlinear time series solutions of the coupled non- linear spectral equations. We have incorporated into our numerical procedure singular value decomposition computer source codes presented by Press *et al.* (pp. 59–65 in [11]). The computational procedure is made up of two parts, the computation of the autocorrelation matrix and the decomposition of that matrix [11]. The computation of the autocorrelation of the fluctuating spectral velocity wave components is accomplished with the particular source code presented by Press *et al.* (pp. 545–546 in [11]). The additional source code presented by Press *et al.* (pp. 66–70 in [11]) for the computation of the singular value decomposition procedure, is also included in the computational process. The overall computational procedure yields the empirical eigenvalues for each of the empirical eigenfunctions for the given nonlinear time series data segment.

The application of the singular value decomposition procedure to a specified segment of the nonlinear time-series solution for the each of the normal and span wise velocity wave components yields the distribution of the component eigenvalues λ_j across the empirical modes, j, for these spectral velocity components. These modes will be simply denoted as empirical modes.

We assume that component eigenvalues, λ_j, yielded by the singular value decomposition method, satisfy the following conditions: first, the eigenvalues are the maximum-liklihood values (pp. 676–681 in [11]); second, the distribution of these eigenvalues is approximately exponential over the empirical modes, j; and third, the summation of the eigenvalues over the empirical modes is unity. Then, the empirical entropy, $Semp_j$, may be defined from these eigenvalues by the expression [17,18]:

$$Semp_j = -\ln(\lambda_j) \tag{47}$$

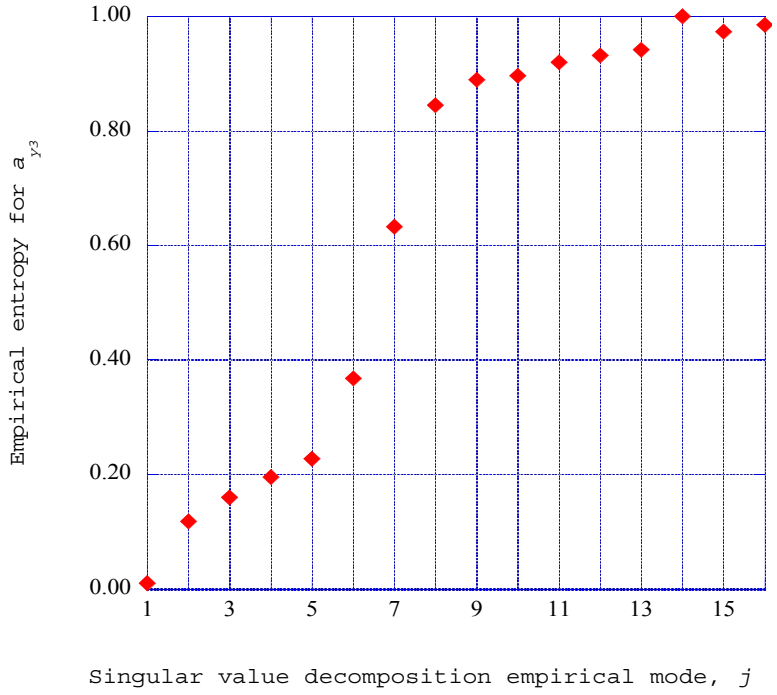

Figure 13. The empirical entropy for the normal spectral velocity wave component, a_{y3}, at the third receiver station x = 0.12 is shown as a function of the singular value decomposition empirical mode number, j.

The empirical entropies for each of the empirical modes from one to sixteen for the normal spectral velocity wave component for the third receiver station at x = 0.12 are shown in Figure 13. The distribution of the empirical entropy over the empirical modes indicates three different characteristics for the nature of kinetic energy within the modes (Isaacson [19]). The initial five eigenmodes contain relatively low levels of empirical entropy, indicating high levels of directed kinetic energy. The following three modes show a steep increase in value, indicating the presence of ordered dissipative structures within the kinetic energy environment. The following eight modes indicate somewhat ordered kinetic energy, with the empirical entropy approaching the maximum of unity in value.

The eigenvalues λ_j represent twice the kinetic energy within each eigenmode distributed across j eigenmode values [20]. The set of eigenvalues obtained for the normal spectral velocity wave component across a specified segment of time series data, consists of an ensemble of data values within the time series, and not as a *sequence* of values.

7. Empirical Entropic Index for Deterministic Spiral Structures

The empirical entropies for the fluctuating normal and span wise spectral velocity wave component time series indicate different characteristics for the various deterministic ensembles within the time series. These results indicate that the majority of the kinetic energy in the deterministic spiral structures for the normal and span wise spectral velocity components is contained within the first five empirical modes of the singular value decompositions, with relatively low empirical entropy. The following three empirical modes indicate deterministic structures. These structures have been classified as coherent [20] with well-defined structural boundaries. To characterize these structures, Tsallis [21] postulated, from fractal concepts, a generalized entropic form

$$S_q = k\frac{1-\sum_{i=1}^{W} p_i^q}{q-1} \qquad \left(\sum_{i=1}^{W} p_i = 1\right) \tag{48}$$

In this expression, k is a positive constant, p_i is the probability of the subsystem to be in the state i, and W is the total number of microscopic possibilities of the system. The Tsallis entropic index, q, would be found from this expression for an ensemble of accessible microscopic subsystems.

The Tsallis entropic form is applicable to an ensemble of microscopic subsystems, while we are working with a set of individual macroscopic systems spread over a limited number of empirical modes, j. In fact, the premise of the computation of the empirical entropy, $Semp_j$ is that this is the entropy of an ordered ensemble described by the empirical eigenvalue, λ_j, for the singular value decomposition empirical mode, j. Hence, we simply adopt, in an *ad hoc* fashion, an expression from which we may extract an empirical index, q_j, from the empirical entropy, $Semp_j$. This expression is written as [17]:

$$Semp_j = -\ln(\lambda_j) = \frac{(\lambda_j)^{q_j} - 1}{(1-q_j)} \tag{49}$$

This expression is simply an artifact that does not have a mathematical basis in non-extensive thermo-statistics. The expression includes the effects of the nonlinear, non-equilibrium nature of the deterministic spiral structures we are following. The expression has the format of an entropic index; hence, we simply call it an empirical entropic index or simply an entropic index.

We have used this expression to extract the empirical entropic index, q_j, from the empirical entropy for the third receiver station at x = 0.12. Figure 14 shows the empirical entropic index for the normal spectral velocity wave component at this station as a function of the empirical mode j. The empirical entropic indices for empirical modes one through six indicate a zero value. Mariz [22], indicates that for an entropic index of zero value, $dSemp_j/dt = 0$. These modes thus contain a high fraction of directed kinetic energy, flowing in the normal direction in a reversible and adiabatic process.

Glandsdorff and Prigogine [23] find that for the general evolution criterion for non-equilibrium dissipative processes, $dSemp_j/dt < 0$. When the Tsallis entropic index is negative, Mariz [22] found that the empirical entropy change is also negative, $dSemp_j/dt < 0$. The results presented in Figure 14 indicate that significant deterministic structures exist within the specified time frame of the nonlinear time series solution. These regions may therefore be classified as ordered, dissipative structures. Therefore, the significant negative nature for the extracted empirical entropic indices from empirical modes seven to sixteen at the third receiver station at x = 0.12 is in agreement with both the Prigogine criterion and the Mariz results for the Tsallis entropic index. The *ad hoc* introduction of an empirical entropy index thus provides a representation of the nonlinear, non-equilibrium spiral structures in a significant way.

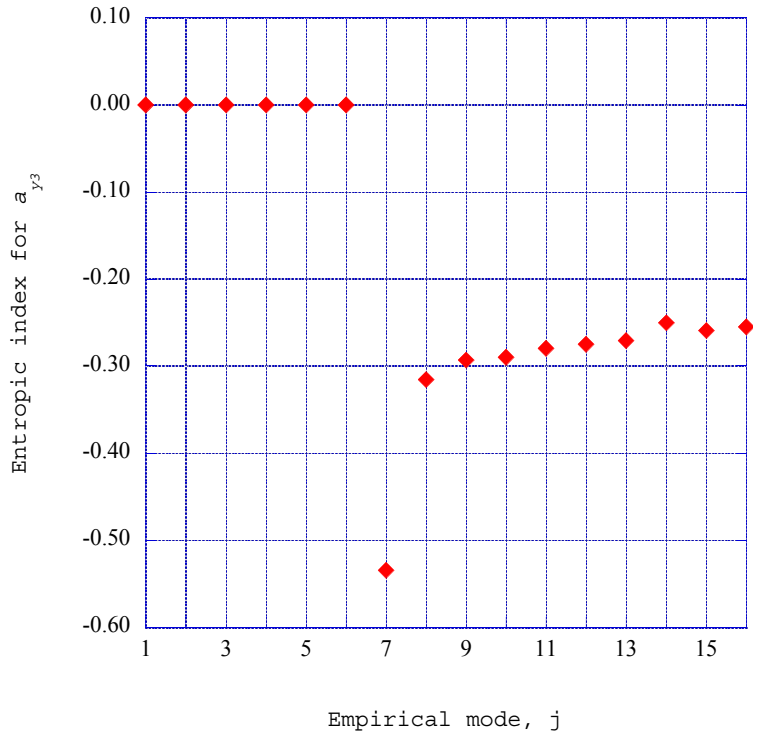

Figure 14. The empirical entropic index for the normal spectral velocity component, a_{y3}, is shown as a function of the empirical mode, j for the third receiver station at x = 0.12.

8. Intermittency Exponents for Deterministic Structures

In this section, we introduce a speculative method to connect the deterministic results for the entropic indices with the final phase of the dissipation of fluctuating kinetic energy into thermodynamic internal energy. We explore this computational connection through the concept of intermittency exponents and a relaxation process into the final thermodynamic entropy state.

The deterministic spiral structures discussed in previous sections are of a macroscopic nature embedded within the nonlinear time series solutions of the nonlinear equations for the fluctuating spectral velocity wave field. Singular value decomposition of the time series solutions provides empirical entropies for these deterministic structures. Empirical entropic indices of the Tsallis form have been extracted from these empirical entropies. We heuristically apply a relationship, found by Arimitsu and Arimitsu [24], connecting the entropic index of Tsallis to the intermittency exponent, ζ_j. This intermittency exponent describes the fraction of fluctuating kinetic energy within the deterministic structure that is dissipated into thermodynamic internal energy. We substitute the absolute value of the empirical entropic index discussed in the previous section into the expression originally derived in [24]. This expression is written as:

$$\left|q_j\right| = 1 - \frac{1 + \zeta_j - \log_2(1+\sqrt{1-2^{-\zeta_j}}) \times \log_2(1-\sqrt{1-2^{-\zeta_j}})}{\log_2(1+\sqrt{1-2^{-\zeta_j}}) - \log_2(1-\sqrt{1-2^{-\zeta_j}})} \tag{50}$$

Given the absolute value of the empirical entropic index, q_j, the intermittency exponent, ζ_j for the mode, j, is extracted from this expression by the use of Brent's method (pp. 397–405 in [11]). The

intermittency exponent for the normal spectral velocity component, a_{y3}, at the third receiver station at x = 0.12 is shown as a function of the empirical mode, *j*, in Figure 15.

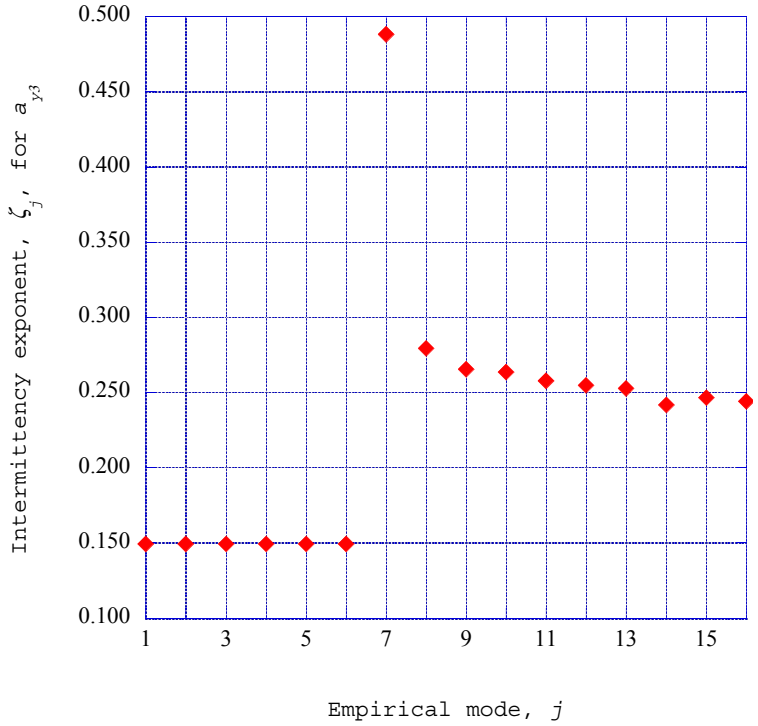

Figure 15. The intermittency exponent for the normal spectral velocity component, a_{y3}, is shown for the third receiver station at x = 0.12 as a function of empirical mode, *j*.

9. Entropy Generation Rates through the Deterministic Spiral Structures

At this point, we are ready to evaluate the entropy generation rate through the deterministic spiral structures produced by the nonlinear interactions within the three-dimensional laminar boundary layer. The local mean flow kinetic energy, $u^2/2$, at the normalized vertical distance, η = 3.00 in the boundary layer, is considered as the source of kinetic energy to be dissipated through the spiral structures.

This available kinetic energy is distributed over the stream wise component, the span wise component and the span wise component. The fraction of kinetic energy in the normal velocity component is denoted as κ_y, with the fraction in the span wise velocity component denoted as κ_z. The rate of dissipation of kinetic energy within each empirical mode of the power spectral energy distribution is denoted as ξ_j. Then the total rate of dissipation of the available fluctuating kinetic energy for the normal and span wise velocity components is the summation, over the empirical modes, *j*, of the product of the kinetic energy fraction of each mode times the intermittency exponent for that mode, ζ_j [25].

The singular value decomposition procedure applied to the nonlinear time series solution for the normal and the span wise velocity wave components yield a distribution of empirical entropic indices across a range of empirical mode numbers for each spectral velocity component. We have extracted corresponding empirical intermittency exponents from these entropic indices for each velocity component over the range of empirical modes. Thus, we have calculated the input energy source for the deterministic spiral structures, the distribution of the dissipation rates of the energy across the

empirical modes of the distribution within the deterministic spiral structures, and the fraction of the energy in each of the empirical modes that dissipates into background thermal energy, thus increasing the thermodynamic entropy.

The equation for the entropy generation rate in an internal relaxation process is provided by the Gibbs equation from thermodynamics (de Groot and Mazur [26]) as:

$$\frac{\partial s}{\partial t} = -J(x)\frac{\partial \mu(x)}{\partial x} \tag{51}$$

In this expression, s is the entropy per unit mass, μ is the mechanical potential for the dissipation of the ordered structures into background thermal energy and $J(x)$ is the net source of the dissipation rates for the ordered kinetic energy available for dissipation.

We consider the dissipation of the ordered structures into background thermal energy as a relaxation process of the stream wise velocity in the initial state to the final equilibrium state of the stream wise velocity over the internal parameter x. At the final equilibrium state, the stream wise velocity of the dissipated structure vanishes. The boundary layer mean velocity may be written, from Equation (11), as $u = u_e f'$. The expression for the entropy generation rate through the deterministic spiral structures may then be written as [25]:

$$\dot{S}_{gen} = \rho\left[\left(\frac{1}{2}\frac{u_e^2}{T}\right)\left(f'\right)^2\left\{\kappa_y\left(\sum_{j=1}^{16}(\xi_j\zeta_j\right)_y + \kappa_z\left(\sum_{j=1}^{16}\left(\xi_j\zeta_j\right)\right)_z\right\}\left(\frac{u_e}{x}\right)\right] \tag{52}$$

Substituting the results of the computational procedures as outline in the previous sections into Equation (52), the resulting value of the entropy generation rate is shown as a single point in Figure 16.

For a comparison of this value for the entropy generation rate, the entropy generation rate within a turbulent boundary layer is computed for each given stream wise location. Following Truitt [27] and Bejan [28], the expression for the entropy generation rate in a turbulent boundary layer may be written, incorporating Equation (8), as

$$\dot{S}_{turb} = \rho\frac{(\upsilon + \varepsilon_m)}{T}\left(\frac{\partial u}{\partial y}\right)^2 \tag{53}$$

Applying the Falkner-Skan transformation, Equation (9), in the differentiation with respect to y and the definition of the term,

$$\varepsilon_m^+ = \frac{\varepsilon_m}{\nu}, \tag{54}$$

the entropy generation rate across the turbulent boundary layer may be written as

$$\dot{S}_{turb} = \rho\left(\frac{1}{2}\frac{u_e^2}{T}\right)\left(f'\right)^2(1+\varepsilon_m^+)(f'')^2\left(\frac{u_e}{x}\right) \tag{55}$$

The computation of the turbulent boundary layer begins at the initial stream wise station x = 0.02 with transition enforced at that location. Hence, the turbulent boundary layer for our calculations at the stream wise location x = 0.12 is much smaller than a naturally occurring transition further along the stream wise direction. The distribution of the entropy generation rates across the turbulent boundary layer at two stream wise stations is shown in Figures 16 and 17. Ghasemisahebi [29] presents the results of a study of the entropy generation process in the bypass transition region of a flat plate

boundary layer under strong levels of free stream turbulence and stream wise pressure gradients, providing insight into the entropy generation process near the flat plate surface.

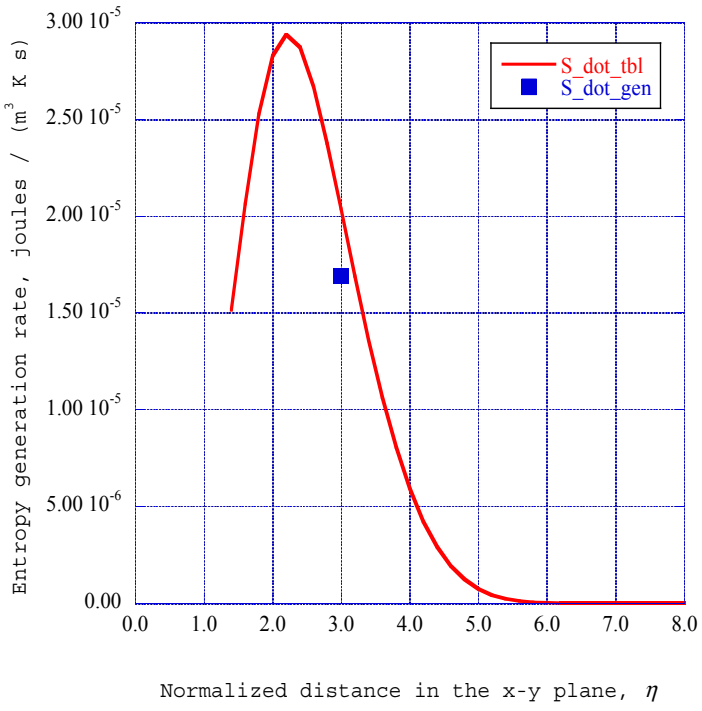

Figure 16. The entropy generation rate for the deterministic spiral structure at x = 0.12 is compared with the entropy generation rates across a turbulent boundary layer as a function of the normalized distance from the horizontal surface.

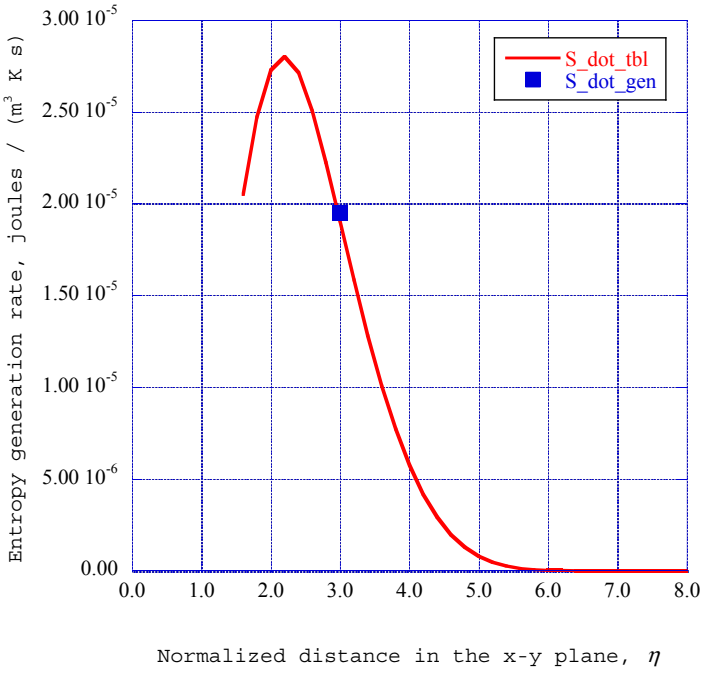

Figure 17. The entropy generation rate for the deterministic spiral structure at x = 0.14 is compared with the entropy generation rates across a turbulent boundary layer as a function of the normalized distance from the horizontal surface.

The entropy generation rates for the turbulent boundary layers are shown in Figures 16 and 17. These results have been computed for the flow, thermodynamic, and transport properties given in Equations (1)–(4). We have included these profiles to provide a set of values of entropy generation rates based on empirical, experimentally obtained turbulent boundary layer computational procedures for comparison with the entropy generation rates obtained for the deterministic spiral structures. At x-axis stations of x = 0.12 and x = 0.14, the values for the entropy generation rates for the spiral structures compare very well with the values for the turbulent boundary layer production rates.

10. Discussion

The boundary layer configuration in a corner flow involves the development of stream wise boundary layers on both the horizontal surface and the vertical surface of the corner structure. The development of the boundary layer in the stream wise direction along the vertical surface provides a crosswind velocity boundary layer in the z-direction that serves as a triggering mechanism for the initiation of deterministic spiral structures within the horizontal surface boundary layer configuration. The three-dimensional orthogonal boundary layer configuration on the horizontal surface is solved for the mean boundary layer velocity gradients using the computational techniques of Cebeci and Bradshaw [6]. The velocity fluctuation equations of Townsend [2] are cast into spectral form and arranged into a Lorenz-type format of coupled nonlinear time dependent equations, with the mean velocity gradients serving as input control parameters. The synchronization properties of Lorenz-type system of equations are used to obtain deterministic spiral instabilities at several x-axis stations.

The initial observation is that the crosswind velocity in the z direction on the horizontal surface serves as a triggering mechanism for the development of deterministic spiral instabilities within the three-dimensional orthogonal horizontal surface boundary layer system. These instabilities appear to be initiated with crosswind velocities of approximately 0.083 in dimensionless units. We have used the Blasius solution crosswind velocity of 0.0867 for the x-axis station at x = 0.06 for the initial or transmitter station and the crosswind velocity of 0.0613 for the third receiver station at x = 0.12.

The crosswind velocity forms a boundary layer in the z-y plane along the horizontal surface in the z direction, thus forming a three-dimensional boundary layer configuration. The solutions of the set of coupled nonlinear spectral equations for this set of orthogonal boundary layers for the initial or transmitter station at x = 0.06 indicate the initiation of somewhat irregular deterministic spiral structures in the stream wise direction. The synchronization properties of the Lorenz type nonlinear equations produce, at the third receiver station at x = 0.12, well-defined deterministic spiral structures.

The computational procedure uses Burg's method [16] to extract the power spectral density for each of the nonlinear time series solutions across a selected time frame within the deterministic spiral structure. A significant result for this calculation is that the stream wise component of the spiral structure appears to be a smooth function without a significant level of power spectral density. Also, the stream wise nonlinear spectral wave component time series solution is not described by the non-extensive statistics used for the analysis of the remaining instabilities. Therefore, the stream wise velocity wave component solution has not been included in the computational procedures.

The method of singular value decomposition [11] applied to selected time frames of the time series solutions for the normal and span wise velocity components yields values for the empirical entropy [19] for a selected range of empirical modes. Empirical entropic indices [19] are extracted from these

empirical entropy values. Using results obtained from the fractal theory of turbulence dissipation [24], the intermittency exponent is extracted for each of the empirical modes identified in the results of the singular value decomposition procedure. An essential aspect of the intermittency exponents is that these exponents represent the fraction of kinetic energy dissipation rate available in each empirical mode that is actually dissipated into background thermal energy of the flow [24].

The source of kinetic energy for the dissipation process is the steady stream wise velocity for the particular boundary layer vertical location. This kinetic energy is distributed into corresponding fractions within the stream wise, normal, and span wise spectral velocity wave components. Excluding the stream wise velocity contribution to the kinetic energy, the normal and span wise spectral velocity components provide a fraction of the total kinetic energy to the dissipation process. That fraction is distributed over the various empirical modes displayed by the power spectral density for each velocity component. Multiplying the fraction of kinetic energy in each empirical mode by the intermittency exponent for that mode yields the dissipation rate for the fraction of kinetic energy in that particular empirical mode. Summing these products over all of the empirical modes for each spectral velocity component yields the net dissipation rate for that component. Finally, the dissipation of kinetic energy for the respective spectral velocity components is found by multiplying the net dissipation rate by the fraction of total fluctuation kinetic energy available in each velocity component.

From concepts of non-equilibrium thermodynamics [26], we obtain an expression for the rate at which the flux of kinetic energy dissipation is converted into thermal internal energy. The entropy generation rate through deterministic spiral structures is found to be the product of the kinetic energy dissipation rate within the structure times the rate of relaxation along internal coordinates into background thermal energy divided by the local absolute temperature. The flow thermal and transport parameters for the given environment allow the entropy generation rate to be computed. The resulting entropy generation rate is compared with entropy generation rates in a weak turbulent boundary layer for these same input parameters and found to be comparable in value.

It should be noted that the formation of the stream wise boundary layer along the horizontal surface also produces a cross wind velocity acting orthogonally on the stream wise boundary layer forming along the vertical surface of the corner flow configuration. We should therefore expect that deterministic spiral structures also form in the boundary layer on the vertical surface. Thus, the overall configuration should yield pairs of counter rotating spiral structures, as indicated by Cebeci and Bradshaw [6].

11. Conclusions

The application of an exploratory computational procedure to the three-dimensional flow in a corner laminar boundary-layer environment predicts the development of deterministic spiral structures within the boundary-layer flow. It has been found that the initial boundary layer along the vertical surface of the right-angle corner provides a triggering crosswind velocity for the generation of fluctuating spiral structures in the horizontal boundary layer flow. Incorporation of the synchronization properties of Lorenz-type equations into the computational procedure yields clearly defined deterministic spiral structures at several downstream stations. The power spectral density distributions for the normal and span wise spectral velocity wave components provide values for the kinetic energy available for dissipation into background thermal energy. The computational procedure includes the

singular value decomposition technique applied to the normal and span wise spectral velocity components yielding empirical entropies, empirical entropic indices, and intermittency exponents across the empirical modes for each component. These properties yield the kinetic energy dissipation rate within each of the deterministic spiral structures. The computational procedure demonstrates that the combination of these rates with the total kinetic energy available for dissipation yields the net rate of dissipation of kinetic energy into background thermal energy within the fluctuating components of the spiral structures. It is shown that concepts from non-equilibrium thermodynamics provide an expression for the overall rate of entropy generation as kinetic energy dissipation occurs within the deterministic spiral structures. The entropy generation rates within the spiral structures computed for several x-axis locations compare well with similar computations for the entropy generation rates for a weak turbulent boundary layer at the same x-axis stations in the corner boundary layer flow.

Conflicts of Interest

The author declares no conflicts of interest.

Nomenclature

a_i	Fluctuating *i-th* component of velocity wave vector
b	Fluctuating Fourier component of the static pressure
b_n	Coefficient in modified Townsend equations defined by Equation (40)
E	Power spectral density for a particular frequency, f
E_{avail}	Available kinetic energy dissipation rate for a given mode
f	Frequency for power spectral density distribution
f_1	Initial frequency in the power spectral density, Equation (46)
f_2	Final frequency in the power spectral density, Equation (46)
F	Time-dependent feedback factor
j	Mode number empirical eigenvalue
j	Spectral entropy segment number
J	Net source of kinetic energy dissipation rate, Equation (51)
k	Time-dependent wave number magnitude
k	Dimensional constant, Equation (48)
k_i	Fluctuating *i-th* wave number of Fourier expansion
K	Adjustable weighting factor
m	Pressure gradient parameter, Equation (12)
n	Time step number, stream wise station number
p	Local static pressure
p_1	Static pressure in the combustion process
p_i	Probability of being in a state i, Equation (48)
q	Tsallis non-extensive entropic index
q_j	Empirical entropic index for the empirical mode, j
r_n	Coefficient in modified Townsend equations defined by Equation (38)
s	Entropy per unit mass

s_n	Coefficient in modified Townsend equations defined by Equation (39)
$Semp_j$	Empirical entropy for empirical mode, *j*
S_q	Tsallis entropy, Equation (48)
$\dot{S}_{gen}$	Entropy generation rate through kinetic energy dissipation
$\dot{S}_{turb}$	Entropy generation rate in a turbulent boundary layer
t	Time
t_i	Inlet temperature for the combustion process
T_{aft}	Adiabatic flame temperature
u	Mean stream wise velocity in the stream wise direction in Equation (5)
u'	Fluctuating stream wise velocity in Equation (5)
u_e	Stream wise velocity at the outer edge of the x-y plane boundary layer
u_i	The *i-th* component of the fluctuating velocity
U_i	Mean velocity in the *i-th* direction in the modified Townsend equations
v	Mean normal velocity in Equation (5)
v'	Fluctuating normal velocity in Equation (5)
w_e	Span wise velocity at the outer edge of the z-y plane boundary layer
W	Total number of microscopic states in a system, Equation (49)
x	Stream wise distance
x_i	*i-th* direction
x_j	*j-th* direction
y	Normal distance
z	Span wise distance

Greek Letters

δ	Boundary layer thickness
δ_{lm}	Kronecker delta
ε_m	Eddy viscosity
ε_m^+	Normalized eddy viscosity
ζ_j	Intermittency exponent for the *j*-th mode in Equation (50)
η	Transformed normal distance parameter
κ	Fraction of kinetic energy defined by Equation (52)
λ_j	Eigenvalue for the empirical mode, *j*
μ	Mechanical potential in Equation (51)
ν_l	Kinematic viscosity of the gas mixture
ξ_j	Kinetic energy dissipation rate in the *j*-th empirical mode
ρ	Density
σ_{yn}	Coefficient in modified Townsend equations defined by Equation (36)
σ_{xn}	Coefficient in modified Townsend equations defined by Equation (37)

Subscripts

e	Outer edge of the x-y plane boundary layer
i, j, l, m	Tensor indices
x	Component in the x-direction
y	Component in the y-direction
z	Component in the z-direction

References

1. Cebeci, T.; Cousteix, J. *Modeling and Computation of Boundary-Layer Flows*; Springer: Berlin, Germany, 2005.
2. Townsend, A.A. *The Structure of Turbulent Shear Flow*, 2nd ed.; Cambridge University Press: Cambridge, UK, 1980.
3. Dorrance, W.H. *Viscous Hypersonic Flow: Theory of Reacting and Hypersonic Boundary Layers*; McGraw-Hill: New York, NY, USA, 1962.
4. Chow, C.-Y. *An Introduction to Computational Fluid Mechanics*; Seminole Publishing Company: Boulder, CO, USA, 1983; pp. 228–238.
5. Hansen, A.G. *Similarity Analyses of Boundary Value Problems in Engineering*; Prentice-Hall: Englewood Cliffs, NJ, USA, 1964; pp. 86–92.
6. Cebeci, T.; Bradshaw, P. *Momentum Transfer in Boundary Layers*; McGraw-Hill: New York, NY, USA, 1977; pp. 319–321.
7. Isaacson, L.K. Spectral Entropy in a Boundary Layer Flow. *Entropy* **2011**, *13*, 1555–1583.
8. Mathieu, J.; Scott, J. *An Introduction to Turbulent Flow*; Cambridge University Press: Cambridge, UK, 2000; pp. 251–261.
9. Manneville, P. *Dissipative Structures and Weak Turbulence*; Academic Press: Waltham, MA, USA, 1990.
10. Pyragas, K. Continuous Control of Chaos by Self-controlling Feedback. In *Controlling Chaos: Theoretical and Practical Methods in Non-linear Dynamics*; Kapitaniak, T., Ed.; Academic Press: Waltham, MA, USA, 1996; pp. 118–123.
11. Press, W.H.; Teukolsky, S.A.; Vetterling, W.T.; Flannery, B.P. *Numerical Recipes in C: The Art of Scientific Computing*, 2nd ed.; Cambridge University Press: Cambridge, UK, 1992.
12. Pecora, L.M.; Carroll, T.L. Synchronization in Chaotic Systems. In *Controlling Chaos: Theoretical and Practical Methods in Non-linear Dynamics*; Kapitaniak, T., Ed.; Academic Press: Waltham, MA, USA, 1996; pp. 142–145.
13. Pérez, G.; Cerdeiral, H.A. Extracting Messages Masked by Chaos. In *Controlling Chaos: Theoretical and Practical Methods in Non-linear Dynamics*; Kapitaniak, T., Ed.; Academic Press: Waltham, MA, USA, 1996; pp. 157–160.
14. Cuomo, K.M.; Oppenheim, A.V. Circuit Implementation of Synchronized Chaos with Applications to Communications. In *Controlling Chaos: Theoretical and Practical Methods in Non-linear Dynamics*; Kapitaniak, T., Ed.; Academic Press: Waltham, MA, USA, 1996; pp. 153–156.
15. Isaacson, L.K. Ordered Regions within a Nonlinear Time Series Solution of a Lorenz Form of the Townsend Equations for a Boundary-Layer Flow. *Entropy* **2013**, *15*, 53–79.

16. Chen, C.H. *Digital Waveform Processing and Recognition*; CRC Press: Boca Raton, FL, USA, 1982; pp. 131–158.
17. Isaacson, L.K. Spectral Entropy, Empirical Entropy and Empirical Exergy for Deterministic Boundary-Layer Structures. *Entropy* **2013**, *15*, 4134–4158.
18. Rissanen, J. *Information and Complexity in Statistical Modeling*; Springer: Berlin, Germany, 2007.
19. Isaacson, L.K. Transitional Intermittency Exponents through Deterministic Boundary-Layer Structures and Empirical Entropic Indices. *Entropy* **2014**, *16*, 2729–2755.
20. Holmes, P.; Lumley, J.L.; Berkooz, G.; Rowley, C.W. *Turbulence, Coherent Structures, Dynamical Stations and Symmetry*, 2nd ed.; Cambridge University Press: Cambridge, UK, 2012.
21. Tsallis, C. *Introduction to Nonextensive. Statistical Mechanics*; Springer: Berlin, Germany, 2009; pp. 37–43.
22. Mariz, A.M. On the Irreversible Nature of the Tsallis and Renyi Entropies. *Phys. Lett. A* **1992**, *165*, 409–411.
23. Glansdorff, P.; Prigogine, I. *Thermodynamic Theory of Structure, Stability and Fluctuations*; Wiley: Hoboken, NJ, USA, 1971.
24. Arimitsu, T.; Arimitsu, N. Analysis of Fully Developed Turbulence in Terms of Tsallis Statistics. *Phys. Rev. E* **2000**, *61*, 3237–3240.
25. Isaacson, L.K. Entropy Generation through a Deterministic Boundary-Layer Structure in Warm Dense Plasma. *Entropy* **2014**, *16*, 6006–6032.
26. De Groot, P.; Mazur, S.R. *Non-Equilibrium Thermodynamics*; Elsevier: Amsterdam, The Netherlands, 1962.
27. Truitt, R.W. *Fundamentals of Aerodynamic Heating*; Wiley: Hoboken, NJ, USA, 1960.
28. Bejan, A. *Entropy Generation Minimization*; CRC Press: Boca Raton, FL, USA, 1996.
29. Ghasemisahebi, E. *Entropy Generation in Transitional Boundary Layers*; LAP LAMBERT Academic Publishing: Saarbrücken, Germany, 2013.